PHOTONICS Research

Giant enhancements of high-order upconversion luminescence enabled by multiresonant hyperbolic metamaterials

Haofei Xu,[1] Zhimin Zhu,[2] Jiancai Xue,[1] Qiuqiang Zhan,[2] Zhangkai Zhou,[1,3] and Xuehua Wang[1,4]

[1]State Key Laboratory of Optoelectronic Materials and Technologies, School of Physics, Sun Yat-sen University, Guangzhou 510275, China
[2]Centre for Optical and Electromagnetic Research, South China Academy of Advanced Optoelectronics, South China Normal University, Guangzhou 510006, China
[3]e-mail: zhouzhk@mail.sysu.edu.cn
[4]e-mail: wangxueh@mail.sysu.edu.cn

Received 4 November 2020; revised 11 January 2021; accepted 11 January 2021; posted 12 January 2021 (Doc. ID 414047); published 1 March 2021

Photonic nanostructures with resonant modes that can generate large electric field (EF) enhancements are applied to enhance light-matter interactions in nanoscale, bringing about great advances in both fundamental and applied science. However, a small hot spot (i.e., the regions with strong EF enhancements) and highly inhomogeneous EF distribution of the resonant modes usually hinder the enhancements of light-matter interactions in a large spatial scale. Additionally, it is a severe challenge to simultaneously generate multiple resonant modes with strong EF enhancements in a broadband spectral range, which greatly limits the capacity of a photonic nanostructure in boosting optical responses including nonlinear conversion, photoluminescence, etc. In order to overcome these challenges, we presented an arrayed hyperbolic metamaterial (AHMM). This AHMM structure is applied to simultaneously enhance the three-photon and four-photon luminescence of upconversion nanoparticles. Excitingly, the enhancement of the three-photon process is 1 order of magnitude larger than previous records, and for the enhancing four-photon process, we achieve an enhancement of 3350 times, greatly beneficial for overcoming the crucial problem of low efficiency in near infrared light upconversion. Our results demonstrated a promising platform for realizing giant enhancements of light-matter interactions, holding potential in constructing various photonics applications such as the nonlinear light sources.

https://doi.org/10.1364/PRJ.414047

1. INTRODUCTION

Boosting light-matter interactions in nanoscale by using photonic nanostructures lies at the heart of photonics-based science and technology, because related studies can not only enrich our basic understandings by discovering novel phenomena (such as room-temperature strong coupling at quantum limit, spaser, and giant nonlinear response) [1–3] but also have brought about advanced applications [4,5]. To enhance light-matter interactions, a large variety of photonic platforms, such as photonic crystals, dielectric microcavities, and plasmonic resonators, have been developed throughout the last decades [6,7], creating great value for various fields ranging from physics, chemistry, biology, and medicine to geology and art, cultivating fruitful applications like surface-enhanced Raman spectroscopy, photocatalysis, biosensors, and photothermal therapy [8–16].

Generally, the resonant modes of photonic structures can greatly enhance the electric field (EF) in hot spots (i.e., the regions with strong EF enhancements), and therefore they are extensively applied to enhance light-matter interactions [17]. Despite the remarkable advances made by the resonant modes, small hot spots and highly inhomogeneous EF distribution of the resonant modes greatly limit their capacity in enhancing light-matter interactions in a large scale. It is also difficult to simultaneously generate multiple resonant modes with strong EF enhancements in a broadband spectral range. This makes it very hard to realize strong optical enhancements simultaneously at the wavelengths of both pumping and radiation, and therefore limits the enhancement effects in various optical processes such as nonlinear conversion and photoluminescence [18–20]. To date, a photonic platform that can simultaneously address these problems is lacking.

To overcome the abovementioned challenges, we propose the arrayed hyperbolic metamaterials (AHMMs) consisting of two-dimensional periodic hyperbolic pillars. Hyperbolic metamaterials (HMMs) are famous for supporting the infinite photonic density of states (PDOS), large EF enhancements, and broadband electromagnetic manipulation [21,22], which

enable the possibility of multiresonant modes in a broadband spectral range. Furthermore, due to the bulk material response [23], the hot spots of their resonant modes can be homogeneously distributed in the interstitial space of adjacent pillars. This also leads to a vast spatial overlapping inside the structure gaps, giving rise to the simultaneous functioning of these modes and benefiting multiwavelength applications. To demonstrate the promising potential of the AHMM, we applied the AHMM to enhance a high-order nonlinear response of rare-earth upconversion nanoparticles (UCNPs). The N-photon upconversion emissions of rare-earth UCNPs, especially the high-order processes (i.e., $N > 2$), offer a wide variety of applications including deep-tissue biophotonics, multioptical coding, and so on [24,25]. However, these high-order nonlinear processes are greatly suffering from their low intensities [26]. Herein, by using the AHMMs, we obtained giant enhancements of high-order nonlinear processes simultaneously (i.e., 1800 and 3350 times luminescence enhancements for three- and four-photon processes, respectively). These results validate the excellent performance of the AHMM in serving as a photonic platform for enhancing light-matter interactions, indicating promising potential in various applications, such as multiple frequency conversion, nanoscale lasers, and quantum information processing [27–30].

2. EXPERIMENT

A. Fabrication of the AHMM Structure

A clean silicon wafer was prepared as the primal substrate. Four pairs of Au and Al_2O_3 layers were alternatively deposited by using electron beam evaporation (Ohmiker-50B), with the thickness of Au and Al_2O_3 layers being ~10 nm and ~20 nm, respectively. The deposition rates of both materials were set to be 1.0 A/s, and the base pressure of the evaporation chamber was 6×10^{-8} Torr (1 Torr = 133.322 Pa). After that, nanopatterns were engraved into the uniform HMM by a focused ion beam system (AURIGA, ZEISS) to form the final structures. The dose of an ion beam was 0.5 nC/μm^2, and the beam current was 50 pA under 30 kV.

B. Synthesis of UCNPs

The designed UCNPs were synthesized following previously reported protocols with some modifications [31–33]. In this synthesis process, a 5 mL $Ln(CH_3CO_2)_3$ (Ln = Y/Yb/Tm) stock solution (0.2 M, 1 M = 1 mol/L) was added into a 100 mL round bottom flask, followed by the addition of 7.5 mL oleic acid (OA) and 17.5 mL 1-octadecene (ODE). The mixture was heated to 150°C under stirring for 40 min to form the lanthanide-oleate precursor solution and then cooled down to room temperature. Then 10 mL of NH_4F-methanol solution (0.4 M) and 2.5 mL of NaOH-methanol solution (1.0 M) were pipetted into a 15 mL centrifuge tube, and then the mixture solution was quickly injected into the flask. Subsequently, the mixture was heated to 50°C and kept at that temperature for at least 0.5 h. Then it was heated to 110°C under vacuum to remove methanol. After the methanol was evaporated, the mixture was heated to 300°C and incubated at that temperature for 1.5 h under an argon atmosphere, and then cooled down to room temperature. The UCNPs were precipitated by the addition of ethanol, followed by centrifugation at 7500 r/min for 5 min. The obtained UCNPs were washed several times using ethanol and cyclohexane and were finally redispersed into cyclohexane for subsequent use.

C. Optical Measurement

Photoluminescence (PL) spectra of the UCNPs were measured by a confocal microspectroscopic system. The pump laser, a continuous wavelength laser at 980 nm, was focused on the sample by a 100× focusing lens (N.A. = 0.9) with a spot size of 3.8 μm in diameter. Then, the photoluminescence from samples was collected through the same focusing lens with a collecting angle of ~65° and a shortpass filter (900 nm) blocking the laser signal. Finally, a spectrometer (Princeton Instruments Acton SP2750) was applied to obtain the PL spectra.

D. Numerical Simulation

The simulation was performed using a commercial software, Lumerical FDTD Solutions. The refractive indexes of Au and Al_2O_3 were from the experimental data of CRC and Palik. The finest mesh size was set to be 0.5 nm inside and near the structure. A dipole source ranging from visible light to near infrared was used to get the Purcell factor (P) and external quantum efficiency (η). The Purcell factor result is equivalent to dividing the power emitted by a dipole source in the environment by the power emitted by the dipole in a homogeneous environment (bulk material), since the emission rate is proportional to the local density of optical states (LDOS), and the LDOS is proportional to the power emitted by the source. The external quantum efficiency of a dipole source was defined as the division of radiative flux to the total photon flux. In FDTD Solutions, we could get the radiative flux by a large enough power monitor set in the far-field (more than a wavelength) and use the transmission box surrounding the dipole at the very near field scale (2 nm) to obtain the total photon flux. Then the value of η was calculated by dividing them. The simulation time was set to 1000 fs to ensure the convergence of the results.

E. Theoretical Calculation for Normalized Dissipated Power Spectra

When a dipole emitter is placed at a distance of h above the planar multilayer with the polarization perpendicular ($\perp$) or parallel ($\parallel$) to the multilayer interface, the normalized dissipated power (P^d) of this dipole can be written as [34,35]

$$\frac{\mathrm{d}P_{\perp}^{d}}{\mathrm{d}u} = \frac{3}{2}\frac{k_0}{k_z}\left(\frac{u}{\sqrt{\varepsilon_1}}\right)^3 (1 + r_p e^{2ik_z h}), \tag{1}$$

$$\frac{\mathrm{d}P_{\parallel}^{d}}{\mathrm{d}u} = \frac{3}{4}\frac{k_0}{k_z}\frac{u}{\sqrt{\varepsilon_1}}\left[1 + r_s e^{2ik_z h} + \frac{k_z^2}{\varepsilon_1 k_0^2}(1 - r_p e^{2ik_z h})\right], \tag{2}$$

where k_0 is the magnitude of the wavevector in a vacuum, $u = k_x/k_0$ is the wavevector component parallel to the multilayer surface normalized by the vacuum wavevector, $k_z = k_0\sqrt{\varepsilon_1 - u^2}$ is the component of the wavevector perpendicular to the multilayer interface, ε_1 is the relative permittivity for the host material, and r_p, r_s are the reflection

coefficient at the interfaces for a p- or s-polarized wave, respectively.

3. RESULT AND DISCUSSION

Figure 1 gives the overview of the properties from the AHMM structure. The schematic configuration of this structure is presented in Fig. 1(a), which consists of alternative metal and dielectric layers with the form of a discrete pillar array. Generally, the dispersion relationship of the anisotropic bulk materials can be represented by the equation inserted in Fig. 1(a) [21]. And for the alternative layers' metastructure, we can calculate the parallel ($\varepsilon_{\parallel}$) and perpendicular permittivity ($\varepsilon_{\perp}$) by the effective medium theory, which is shown by the inset of Fig. 1(b) [22]. When the real part of the two comes to be opposite signs, the AHMM structure can be regarded as a bulk material with hyperbolic dispersion (blue area).

With the consideration of our mature fabrication techniques, we set the thicknesses of Au and Al_2O_3 layers as 10 nm and 20 nm, respectively. Therefore, one can calculate that the hyperbolic region begins from 540 nm, where the AHMM shows much better performance in boosting light-matter interactions over uniform HMM. Similar to previous studies [36,37], the enhancement of the light-matter interaction discussed in this paper is also described by calculating the Purcell factor of a quantum emitter (QE, which is a dipole source) placed near our studied metamaterials [Fig. 1(c)]. In contrast with the results obtained by placing the QE near uniform HMM, the QE located in the gap of AHMM exhibits higher Purcell factors, and the value of the Purcell factors reaches multiple peaks under varied QE wavelengths. These peaks actually correspond to the resonant modes of HMM, which represent propagating modes within the HMM that result from hybridization of the individual surface plasmon polariton (SPP) modes associated with each metal-dielectric interface [38]. To further understand the broadband Purcell response, the normalized dissipated power spectra are calculated. Figure 1(d) shows the normalized dissipated power spectra for a perpendicular dipole placed 10 nm above the hyperbolic Au–Al_2O_3 multilayer surface. The emission wavelength of this dipole varies from 450 nm to 1000 nm, and the calculation methods for the dissipated power with the varied wavelength are given in Section 2.E. The Purcell factor of a dipole can be calculated by integrating its dissipated power from 0 to ∞ wavevector [34,35]. For example, the Purcell factor of a dipole with an emission wavelength at 900 nm can be obtained by integrating the data marked by the white line in Fig. 1(d). As shown by Fig. 1(d), one can find that except for the spectral range around the instinct plasmon mode of Au at about 530 nm, the large dissipated power can also be found over a broadband spectral region in the high wavevector region (i.e., the top-right corner marked by a white-dashed line), which is a unique character for hyperbolic nanostructures [34]. Owing to the existence of this large dissipated power in the top-right corner, the hyperbolic multilayer can support large Purcell factors in a broadband spectral range. In short, the optical behavior of our AHMM can be attributed to the Bloch-like gap plasmon polaritons with high modal confinement inside the multilayer [37–39].

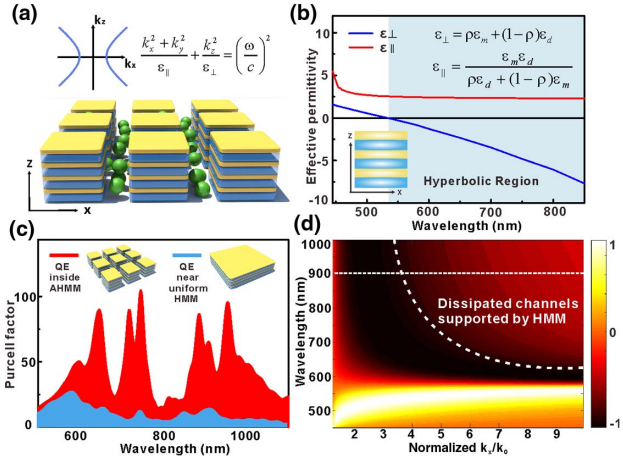

Fig. 1. Novel properties of AHMM. (a) Schematic configuration of a nanopatterned Au–Al_2O_3 multilayer HMM with emitters inside the gaps. Multilayers consist of Au–Al_2O_3 stacks with a thickness period of 10 nm and 20 nm, and four periods in total. Whole structure dispersion relationship is shown in the above illustration. (b) Hyperbolic region of the AHMM. Alternative metal and dielectric, with thickness far smaller than the wavelength, are used to form the structure. Effective parallel ($\varepsilon_{\parallel}$) and perpendicular permittivity ($\varepsilon_{\perp}$) are given by the two formulas inserted. When they are with the opposite sign, the dispersion of the body structure transforms from elliptical to hyperbolic (blue area). ε_m and ε_d represent the dielectric constant of the metal and the medium, respectively, and ρ is the filling ratio of the metal. (c) Purcell factor calculation for a dipole placed in the AHMM gaps (red line) and near the uniform HMM (blue line). High intensity of Purcell factor and multiwavelength-enhanced modes are revealed in the AHMM situation. (d) Normalized dissipated power spectra for a perpendicular dipole at a distance of $h = 10$ nm above a uniform Au–Al_2O_3 multilayer HMM. The color scales indicate normalized dissipated power intensity (on a logarithmic scale).

In addition, the numerical simulation results of the EF distribution inspired by the plane wave prove the high quality of the EF enhancement clearly [Fig. 2(a)]. In the hyperbolic region, one can see that most of the enhanced hot spots are distributed inside the gap between the two adjacent pillars instead of the up or bottom surfaces, and this kind of distribution is quite homogeneous and extensive in space. (The EF distribution is obtained at one resonant mode of 980 nm, and the gap distance is 90 nm.) Moreover, if the gap distance is further reduced to 40 nm, the EF enhancement can be more intense and uniform [Fig. 2(b)]. In this situation, the EF distribution with stronger intensity almost fills the gap space. As a comparison, the EF distributions of the pure Au pillar array with the same size of 40 nm at resonance of 830 nm are also calculated [Fig. 2(c)]. We can see that the EF enhancement is relatively weak, and the hot spots are mainly localized around the edges of pillars, which is not favorable for efficient applications. More intuitively, the gradient of the EF to the space can be used as the figure-of-merit (defined as Q) to describe the uniformity of EF enhancements (i.e., hot spot), so $Q = 0$ means the most uniform EF distribution. As an example, we extracted the EF distribution data in Fig. 2(a) and calculated its Q value [Fig. 2(d)]. It is found that Q can be 0 within a space over 120 mm × 70 mm × 60 nm [marked by the gray rectangle in Fig. 2(a)], indicating a large space of a uniform hot spot.

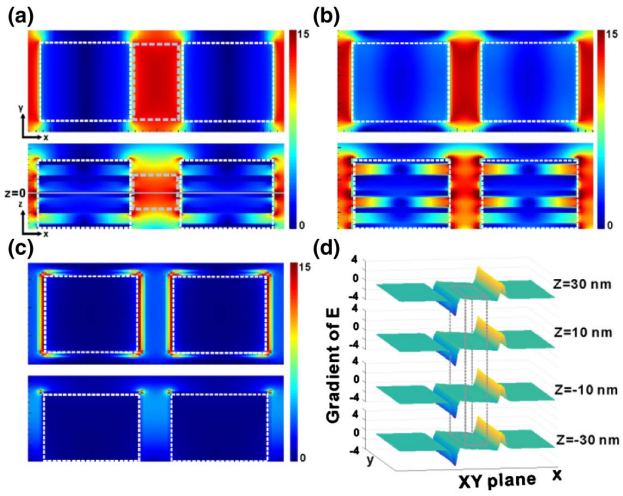

Fig. 2. Electric field distribution of AHMM. (a) Electric field distribution of the AHMM in XY and XZ planes within two cells inspired by plane wave in hyperbolic region (at 980 nm). Extensive EF hot spots are spread over the gap homogeneously. The array is with period of 220 nm and side length of 130 nm (i.e., gap distance of 90 nm). (b) Electric field distribution of the AHMM in XY and XZ planes with smaller gap (40 nm). A stronger and more homogeneous field distribution is formed as the gap becomes smaller. (c) Electric field distribution of the pure Au pillar array with the same size as in (b) XY and XZ planes (resonance 830 nm). (d) Gradient of electric field intensity from (a) in XY plane. Four gradients of XY plane are calculated with different Z values (position "$Z = 0$" is marked in (a) with gray solid line).

It should be mentioned that luminescence nanomaterial involved in a light-matter interaction system usually has an instinct size, which may be hundreds and thousands of cubic nanometers. Therefore, if the hot spot of a photonic mode is smaller than the involved nanomaterial, the effect of the optical enhancement will be remarkably reduced. Herein, the obtained hot spot in our AHMM is obviously larger than most of previous studies [3,6,8] and therefore greatly beneficial for improving the enhancement of light-matter interactions.

Further investigations on the manipulation of resonant modes of AHMM are systematically performed. First, we made the position of the QE fixed in the center of the gap and varied the structure parameters of AHMM. Without the loss of generality, two structural parameters are fixed. One is the total layer number of Au and Al_2O_3 nanofilms, and the other is the gap distance [i.e., d in Fig. 3(a)]. Herein, we use eight alternative layers of Au and Al_2O_3 nanofilms to build the hyperbolic pillar (four layers, respectively, for Au and Al_2O_3), since such a parameter is the threshold for forming hyperbolic dispersion. On the other side, it is calculated that the parameter d only influences the intensity of EF enhancement (smaller d brings about larger EF enhancement), and its variation does not affect the resonant wavelength. Considering the size of the experiment sample of UCNP, the d is set as 90 nm. Therefore, in the analysis presented in Fig. 3, only the variations of parameter a_1 and a_2 are considered. [They are the side length of an individual pillar and are marked in the Fig. 3(a).] Figure 3(b) shows the Purcell factor of a QE inside the AHMM with $a_1 = a_2 = 130$ nm, where the three peaks are labeled as order

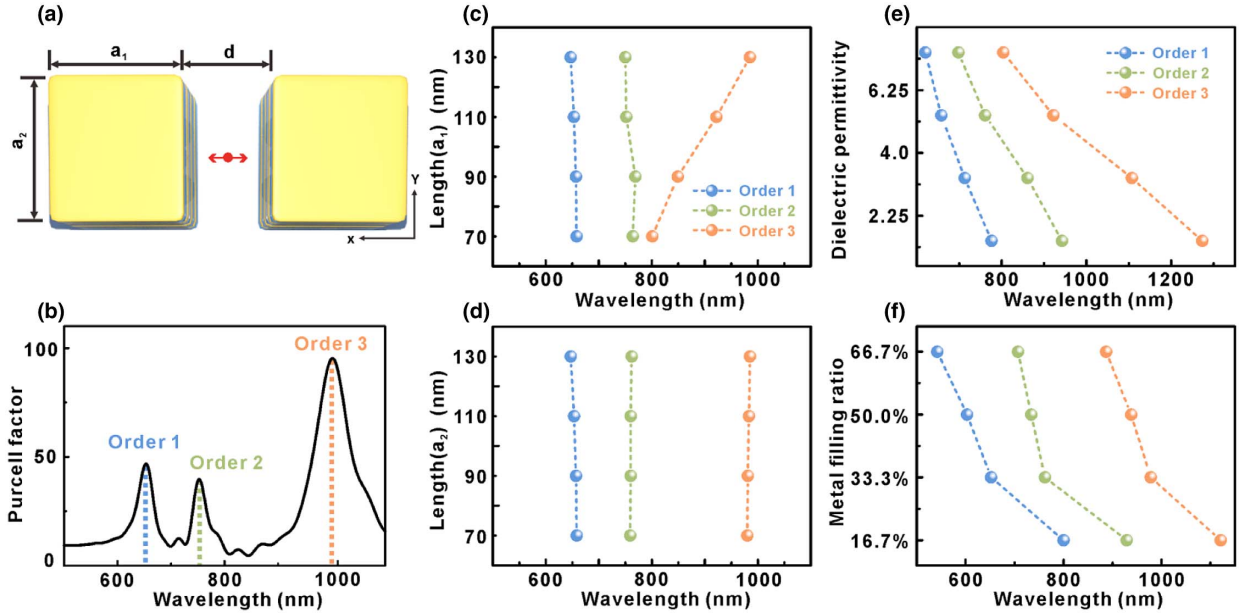

Fig. 3. Theoretical calculation of Purcell factor with different AHMM parameters. (a) Schematic of the AHMM structure in XY view. Dipole is placed at the center inside the gap, and the polarization is parallel to the X axis. Side a_1 and a_2 represent being parallel and perpendicular to the polarization direction of the dipole. (b) Purcell factor of the dipole with $a_1 = a_2 = 130$ nm, $d = 90$ nm. Three obvious peaks, which correspond to the HMM modes, at 650 nm, 745 nm, and 980 nm are labeled in the order 1, 2, 3, respectively. (c) and (d) Distribution of three modes varies with side length of cell: (c) changing the side length of a_1; (d) changing the side length of a_2. There are individually adjustable modes by introducing pattern. (e) and (f) Distribution of three modes changes with HMM constituent: (e) changing the permittivity of dielectric; (f) changing the metal filling ratio. As the nature of the AHMM structure changes, all three modes move subsequently.

1, 2, and 3, respectively. When we evenly vary the length of a_1 (parallel to the polarization direction) from 70 nm to 130 nm, one can see that the peaks of orders 1 and 2 basically do not move, while the third peak shows a linear red shift [Fig. 3(c)]. On the other hand, with the changing of a_2 (perpendicular to polarization direction), the positions of three peaks are almost stable. These phenomena indicate that the modes of orders 1 and 2 result from the instinct resonant modes of HMM, which are mainly dependent on the constitution of HMM. Meanwhile, the mode of order 3 is attributed to the specific array pattern of our AHMM, so changing the structural parameter can modulate its resonant wavelength. Furthermore, the whole positions of these resonant modes can be tuned by adjusting the constitution of the AHMM, such as the dielectric constant [Fig. 3(e)] and the filling ratio of the metal [Fig. 3(f)].

Next, we fixed the structure parameters of AHMM (Au thickness = 10 nm, Al_2O_3 thickness = 20 nm, $a_1 = a_2 = 130$ nm, $d = 90$ nm) and changed the position of the dipole in the calculations. As shown in Fig. 4(a), we selected three typical positions where the dipole is at the center of the upper surface of the pillar, above the gap, and inside the gap, represented by position 1, 2, and 3, respectively. It can be clearly seen that the overall Purcell factor intensity of position 1 is at a relatively low level from Fig. 4(b). When it comes to position 2, two peaks (650 nm and 980 nm) appear with a wide bandwidth. As for position 3, the three peaks in the Purcell enhancement show up together, and the intensity is much higher than that at position 1. Finally, by selecting a spatial location around the cell, a Purcell factor mapping image has been drawn. The results show that there are very few hot spots in the up or bottom of the cell, and most of them are inside the gap. The closer to the cell boundary, the greater the intensity is, with a maximum reaching about 500 times. Another advantage is that the hot spots in the gap work at multiwavelengths, which correspond to the multi high-k modes mentioned above. Besides, the spatial distributions of the Purcell enhancements are well overlapped in these resonant modes, bringing about promising potential for them to work simultaneously in multiwavelength applications like nonlinear energy conversion [40].

We use electron beam evaporation and focused ion beam (FIB) to manufacture the AHMM structure. As shown in Fig. 5(a), in step 1, we overlay Au and Al_2O_3 eight times on the silicon substrate to form a uniform HMM substrate. In step 2, the pillar patterns are directly carried out on the uniform HMM substrate by FIB milling to obtain the final structure. Figure 5(b) and the inset are the SEM images of AHMM at different magnification. Under extremely high magnification, we can clearly see the substructure of HMM with eight alternative layers in total and confirm that the size and gap have reached the requirements of our theoretical design. Next, we use the spin-coating method to make UCNPs fall into the AHMM's gap. It should be noted that due to the spacing of the AHMM arrays, the particles' distribution density with the same concentration (C_0: 12.5 mmol/L) of UCNPs on the AHMM structure is different from that on the blank silicon substrate. For strict comparison of the subsequent fluorescence enhancement test, we made statistics of the average counts, as shown in Fig. 5(c), of particles on the AHMM and the silicon substrate within an excitation laser spot size [the purple circle area in Fig. 5(d)]. At the same concentration, the average number of particles on the silicon substrate is more than that in the AHMM; when we dilute it 10 times, a similar particle number distribution can be obtained. The SEM images of the particles on different substrates are shown in Fig. 5(e), and the agglomeration effect of particles on the nonstructured substrate in Fig. 5(e) (panel ii) explains the differences.

After the sample preparation, we turn to the emission enhancement measurement. Herein, the UCNPs with $NaYF_4$:40%Yb/8%Tm@$NaYF_4$ are chosen as the emitters coupling with the AHMM, and the specific energy level structure of this UCNP is shown in Fig. 6(a). In upconversion

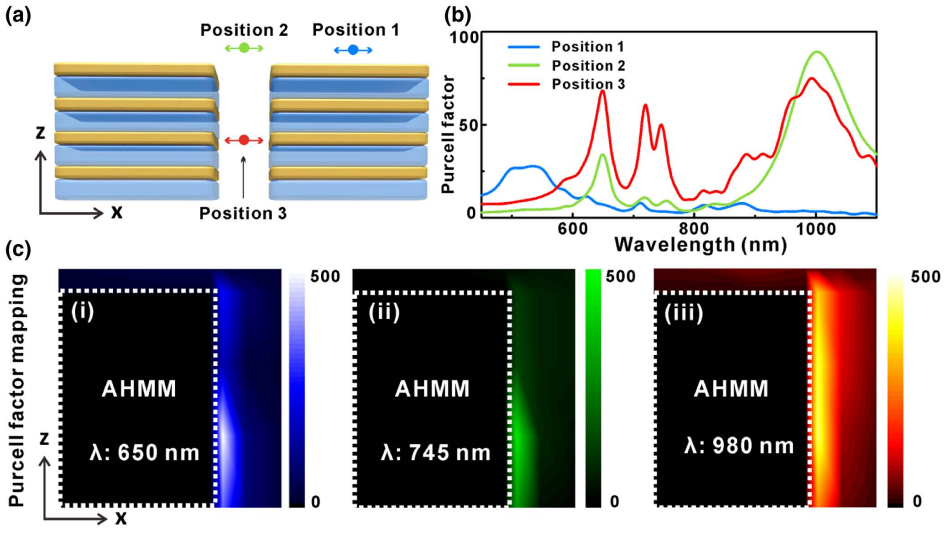

Fig. 4. Theoretical calculation of Purcell factor with different dipole positions. (a) Schematic of the AHMM in XZ view. Three representative positions of dipole are marked in the picture. (b) Purcell factor of dipole at different positions that correspond with (a). More enhanced modes can be found only when emitter is placed inside the gap of AHMM. (c) Spatial mapping of Purcell factor enhancement around the cell at three different wavelengths of the modes. Polarization of the used dipole is parallel to the X direction.

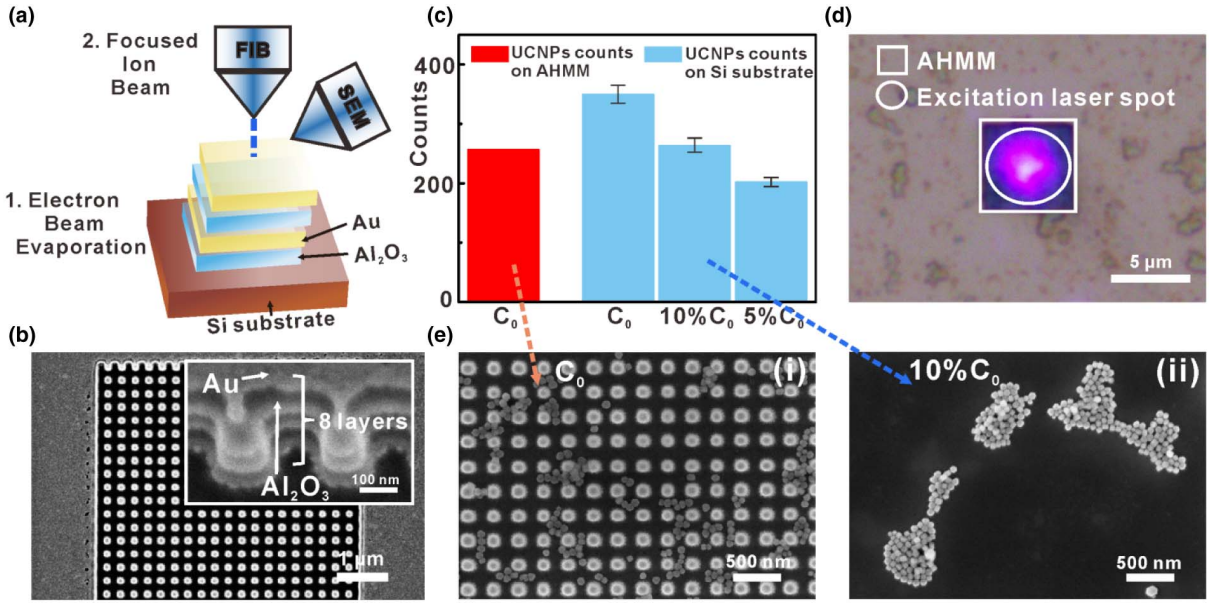

Fig. 5. Preparation and characterization of samples. (a) Schematic of the fabrication process with electron beam evaporation and focused ion beam technology. (b) SEM image of AHMM structure at different magnification. Eight alternative layers can be seen clearly from insert. Roughness in the edge of array is mainly caused by the deposition and milling technology conducted at the subhundred nanometer scale. (c) Statistics of nanoparticle counts on silicon substrate and AHMM with different concentrations. (d) Optical microscope photograph including the AHMM with an excitation laser spot under 100× objective lens. (e) SEM image of UCNPs on (i) AHMM and (ii) silicon substrate with concentration C_0 (12.5 mmol/L) and 10%C_0, respectively. The area of view field is approximately the same as the laser spot in (d).

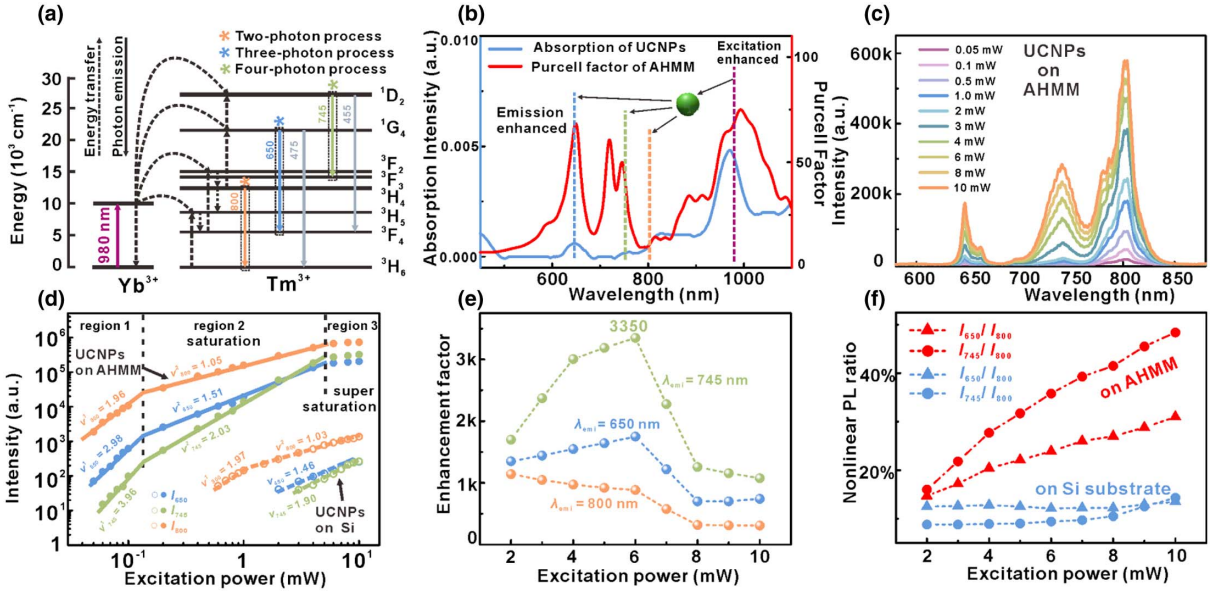

Fig. 6. Experimental emission measurements for UCNPs on different samples. (a) Upconversion mechanism in Yb^{3+}/Tm^{3+} co-doped UCNPs under 980-nm excitation. (b) Design idea of AHMM. Blue solid line is the absorption spectrum of UCNPs, and red solid line is the Purcell factor of a dipole in AHMM. Peaks of Purcell factor are designed to match the excitation and emission wavelengths of the three- and four-photon processes. (c) Spectra of UCNPs on AHMM structure. Excitation power varies from 0.05 mW to 10.0 mW. (d) Excitation power dependence of UCNPs' emission intensity presented in logarithm scale. Top left, UCNPs on AHMM; bottom right: UCNPs on Si substrate. (e) Enhancement factor of the upconversion processes. Descent occurs at 6.0 mW because the UCNPs on AHMM enter the supersaturation stage, while the UCNPs on Si substrate remain in the saturation region. (f) Emission ratios of 650 nm (triangle) and 745 nm (circle) to 800 nm on silicon substrate (blue line) and AHMM structure (red line). Ratios remain basically unchanged on the blank substrate and improve significantly in the AHMM structure as the power increases.

luminescence of this system, the excitation process is attributed to Yb^{3+}, which mainly absorbs photons with a wavelength of 980 nm. The Yb^{3+} can absorb two, three, or four photons at one time, and then transfer its energy to Tm^{3+}, which emits light at wavelengths (λ_{emi}) of 800 nm, 650 nm, and 745 nm (the transition channels are highlighted by star markers), corresponding to the two-, three- and four-photon processes, respectively [41–44]. Figure 6(b) further demonstrates the basic principle for enhancing the emission of UCNPs via AHMMs. As shown by the absorption spectrum of the UCNPs [blue solid line in Fig. 6(b)], the peaks are approximately distributed at 650, 745, 800, and 980 nm. In this paper we focus on the emission enhancements of the three- and four-photon processes; therefore, the Purcell enhancement peaks of AHMM are designed at 650 nm and 745 nm to match the three-photon and four-photon emission wavelengths. Meanwhile, the AHMM also has a Purcell enhancement peak of 980 nm, in accordance with the excitation wavelength of UCNPs. It should be mentioned that from the perspective of application [24–26,45–47], high-order upconversion emissions (i.e., N-photon nonlinear process with $N > 2$) are more favorable than two-photon luminescence due to their larger frequency conversion range, deeper penetration, etc. However, the high-order processes suffer greatly for their lower generation efficiency; thus, it is highly desired to enhance the high-order upconversion emissions.

In order to strictly study the emission enhancing effect, we measured UCNPs with nearly the same particle number on the AHMM and Si substrate. Typical emission spectra of UCNPs on AHMM are presented in Fig. 6(c), where three emission peaks with $\lambda_{emi} = 800$ nm, 650 nm, and 745 nm can be clearly observed. Through extracting the peak value with the corresponding power separately and taking them in logarithm, one can see that the slopes ($\upsilon = \partial \log I / \partial \log P_{exc}$, where I and P_{exc} are the intensity of unconversion emission and excitation power, respectively) of the fitted curves are about 2, 3, and 4 when P_{exc} is below 0.15 mW (defined as region 1), presenting strong evidence for the two-, three-, and four-photon luminescence [Fig. 6(d)] [44]. Also, it is well-known that the upconversion luminescence of rare-earth UCNPs exhibits the phenomenon of saturated absorption, which has also been observed from Fig. 6(d). Since the number of ions in UCNPs that can be excited from the ground state is finite, when the P_{exc} exceeds a threshold, it is reasonable to find that almost all the ions have been pumped to the excited state. In such a case, the number of photons absorbed by UCNPs will be reduced. Thereby, the υ value will gradually decrease with the increasing of P_{exc}. In Fig. 6(d), except for region 1 when the UCNPs are unsaturated with excitation light, another two regions can be observed. For one region, the υ values are basically reduced to half of the original ones (P_{exc} varying from 0.15 mW to 6 mW), suggesting that the UCNPs enter a saturated state (defined as region 2). For another, as the P_{exc} continues to increase (region 3, beyond 6 mW), the υ values of all the three curves further reduce until they are close to 0, indicating that the UCNPs have reached a supersaturated state, and the UCNPs no longer absorb more photons no matter how much the P_{exc} increases.

For the UCNPs on the Si substrate, the phenomenon of saturated absorption can also be noticed. When the excitation is lower than 1.4 mW, one can find the υ of two-photon upconversion (i.e., $\lambda_{emi} = 800$ nm) is 1.97. In this P_{exc} range, the intensity of three- and four-photon emissions is too weak to read, so their results are blank. With the increasing of P_{exc}, υ of two-photon upconversion decreases to 1.03, and we can observe the three- and four-photon emissions with measured υ of 1.46 and 1.9, respectively. Based on these results, one can conclude that the saturation threshold of UCNPs on the Si substrate is 1.4 mW, which is nearly 1 order of magnitude larger than that of UCNPs on AHMM. The huge decreasing of the saturation threshold caused by AHMM results because the AHMM can increase excitation efficiency by creating higher pumping photon flux to excite Yb^{3+} to the excite state [41]. Note that after our samples have experienced the PL measurements with P_{exc} increasing from low to high, its spectral intensity is reproducible under the same P_{exc}. This fact indicates that the applied excitation light has not damaged our samples.

Following the discussion of the saturation threshold changing caused by AHMM, we go further to investigate the emission intensity enhancements of UCNPs enabled by AHMM. The enhancement factor is defined as the ratio of emission peak value of UCNPs on AHMM to that of UCNPs on the Si substrate [Fig. 6(e)]. One can find that all the three multiphoton upconversion emissions have been enhanced by the AHMM. However, since the three- and four-photon processes (i.e., $\lambda_{emi} = 650$ nm and 745 nm) have optical enhancement at both excitation and emission wavelengths, their enhancement factors are obviously larger than that of the two-photon process (i.e., $\lambda_{emi} = 800$ nm). The three-photon and four-photon processes achieved the highest enhancements of 1800 and 3350 times, respectively. Compared to previous studies, our enhancement result of the three-photon process in rare-earth UCNPs systems is 1 order of magnitude larger [48–51]. Furthermore, we obtained a record for the enhancement of the four-photon process (the related reports of four-photon process enhancement in rare-earth UCNPs systems are rare), providing an effective and inspired way for the future study of this field. In addition, one can see that the emission enhancement factors have a large decline when the P_{exc} is over 6.0 mW. The reason is that UCNPs on AHMM enter the supersaturation state under such high P_{exc}, and the υ values of their multiphoton processes become smaller than that of UCNPs on the Si substrate [see Fig. 6(d)]. Since the enhancement factors of three- and four-photon emissions are larger than that of two-photon upconversion, the luminous intensities of three- and four-photon emissions gradually increase to a level comparable to the two-photon process for the UCNPs on our AHMM. More digitally, we use the two ratios of I_{650}/I_{800} and I_{745}/I_{800} to describe this tendency. The different colors (red and blue) and symbols (circle and triangle) represent the ratios of three- and four-photon processes in the silicon substrate and AHMM in Fig. 6(f). It is intuitional that the blue line is always maintained at about 12%, while the red line increases from 14% to 50% as the power increases, indicating that our AHMM structure does help improve the efficiency of the high-order nonlinear process.

In order to more clearly reveal the emission enhancing origin in our AHMM system, the theoretical enhancement factors for the three- and four-photon emissions are theoretically analyzed. In our system, the emission enhancement (f) can be given by $f \propto f_{exc} \cdot f_{emi}$, where the f_{exc} and f_{emi} are the enhancement factors at excitation and emission wavelengths, respectively. In the nonlinear upconversion process, the f_{exc} follows the relationship of $f_{exc} \propto I^N \propto E^{2N}$, where I is the intensity of excitation light, E is the EF enhancement, and N equals the fitting slope of the emission intensity-excitation power dependence curve in a double logarithm (i.e., the parameter υ mentioned in this paper) [52,53]. On the other hand, the Purcell factor is proportional to the imaginary part of Green's function in a medium [36], and it can be regarded as $P(\omega) = \mathrm{Im}\, G(r,\omega) \propto E^2$. Therefore, the f can be given as $f \propto P_{exc}^N \cdot P_{emi}$, where P_{exc} and P_{emi} are the Purcell factors at the excitation and emission wavelengths, respectively. In addition, the absorption of AHMM should be considered. So, adding the external quantum efficiency (η), we considered the theoretical f in our system follows the relationship of $f \propto P_{exc}^N \cdot P_{emi} \cdot \eta$. The values of η are obtained by FDTD simulations, and detailed calculation methods are given in Section 2.D.

Based on our experimental results, the three- and four-photon processes actually occurred when the UCNPs are in the saturated region. According to their υ values, one can find that N should be 1.5 and 2 for the three- and four-photon processes. Thus, taking the values of P_{exc}, P_{emi}, and η at the required wavelengths [η at 650 nm and 745 nm are 4.8% and 1.3%, respectively; the values of P are given in Fig. 6(d)], the f for three- and four-photon emissions [i.e., $f(650)$ and $f(745)$] can be calculated as 2570 and 4580, respectively. These results are quite near the experimental results. Furthermore, we can compare the ratio of $f(745)$ to $f(650)$ from both the theoretical and the experimental aspects, and find the values are also quite similar (1.78 and 1.86, respectively). The good agreement of the theoretical and experimental results further confirms the correctness of our work. It is noticed that improving emission directivity can also enhance emission intensity. However, in our cases, we calculated the emission directivity of a point source (i.e., a dipole) placed on a Si substrate and the middle of AHMM, and find that over 92% power radiated from this dipole is confined in a radiation angle of 65° and 38°, respectively. Since the collecting angle of our optical measurement system is ~65°, it can be concluded that the improvement of emission directivity caused by AHMM only has limited contributions to the emission enhancement.

4. CONCLUSION

In summary, we demonstrated a novel AHMM structure with large and multiple resonant modes for boosting light-matter interactions. Besides, this AHMM structure not only enables homogeneous hot spots in the gap region but also makes the hot spots overlap well in space for different resonant modes. We applied the AHMM structure to simultaneously enhance the high-order nonlinear emissions of UCNPs. The enhancement of the three-photon process is 1 order of magnitude larger than previous records in the three-photon enhancement of rare-earth UCNPs, and we even achieve a 3350 times enhancement of four-photon emission. The reasons for these unprecedented results can be attributed to two advantages of our AHMM. First, the EF distributions of various hot spots in AHMM are homogeneous in the spatial area, providing an environment of strong EF enhancement covering the whole UCNP inside the AHMM. Second, the hot spots are extremely overlapped in space for resonant modes matching the excitation and emission wavelengths of the nonlinear optical process, ensuring the two resonant modes function simultaneously. Our findings demonstrated a promising platform for the giant enhancement of light-matter interaction, which has potential to construct a high-efficiency nonlinear light source and multiplex photonic devices, providing new thoughts in designing functional photonic nanostructures.

Funding. National Key Research and Development Program of China (2016YFA0301300); National Natural Science Foundation of China (11974437, 91750207, 11761141015, 11974123); Key Research and Development Program of Guangdong Province (2018B030329001); Guangdong Special Support Program (2017TQ04C487); Guangdong Natural Science Funds for Distinguished Young Scholars (2017B030306007, 2018B030306015); Guangdong Provincial Natural Science Fund Projects (2019A050510037); Pearl River S&T Nova Program of Guangzhou (201806010033); Open Fund of IPOC (BUPT) (IPOC2019A003); Fundamental Research Funds for the Central Universities (20lgzd30).

Acknowledgment. X.H.W. and Z.K.Z presented the concept, conceived the research outline, and supervised the project. H.F.X. performed the sample fabrications, characterizations, and optical measurements. Z.M.Z and Q.Q.Z. synthesized the UCNPs. H.F.X made the numerical simulations. H.F.X., Z.M.Z., Z.K.Z., J.C.X., and Q.Q.Z. analyzed the theoretical and experimental results. H.F.X., J.C.X., Z.K.Z., and X.H.W. co-wrote the paper with inputs from all the authors. All the authors discussed the results.

Disclosures. The authors declare no conflicts of interest.

REFERENCES

1. N. Rivera and I. Kaminer, "Light-matter interactions with photonic quasiparticles," Nat. Rev. Phys. **2**, 538–561 (2020).
2. S. I. Azzam, A. V. Kildishev, R. M. Ma, C. Z. Ning, R. Oulton, V. M. Shalaev, M. I. Stockman, J. L. Xu, and X. Zhang, "Ten years of spasers and plasmonic nanolasers," Light Sci. Appl. **9**, 90 (2020).
3. N. S. Mueller, Y. Okamura, B. G. M. Vieira, S. Juergensen, H. Lange, E. B. Barros, F. Schulz, and S. Reich, "Deep strong light-matter coupling in plasmonic nanoparticle crystals," Nature **583**, 780–784 (2020).
4. R. Chen, T. D. Tran, K. W. Ng, W. S. Ko, L. C. Chuang, F. G. Sedgwick, and C. C. Hasnain, "Nanolasers grown on silicon," Nat. Photonics **5**, 170–175 (2011).
5. S. W. Lee, S. Bae, D. Kim, and H. S. Lee, "Historical analysis of high-efficiency, large-area solar cells: toward upscaling of perovskite solar cells," Adv. Mater. **32**, 2002202 (2020).
6. A. G. Curtop, R. Quidant, M. P. Kreuzer, N. F. van Hulst, G. Volpe, and T. H. Taminiau, "Unidirectional emission of a quantum dot coupled to a nanoantenna," Science **329**, 930–933 (2010).

7. X. Y. Zhang, Q. T. Cao, Z. Wang, Y. X. Liu, C. W. Qiu, L. Yang, Q. H. Gong, and Y. F. Xiao, "Symmetry-breaking-induced nonlinear optics at a microcavity surface," Nat. Photonics **13**, 21–24 (2019).
8. T. Wang, D. P. Qi, H. Yang, Z. Y. Liu, M. Wang, W. R. Leow, G. Chen, J. C. Yu, K. He, H. W. Cheng, Y. L. Wu, H. Zhang, and X. D. Chen, "Tactile chemomechanical transduction based on an elastic microstructured array to enhance the sensitivity of portable biosensors," Adv. Mater. **31**, 1803883 (2019).
9. Y. Y. Xia, J. Wang, Y. B. Zhang, Y. W. Shan, Y. Y. Dai, A. Chen, T. Y. Shen, S. W. Wu, X. H. Liu, L. Shi, and J. Zi, "Transmission-type optical modulator based on graphene plasmonic resonator integrated with off-resonant Au structure," Adv. Opt. Mater. **8**, 2000264 (2020).
10. Y. J. Bao, Y. Yu, H. F. Xu, C. Guo, J. T. Li, S. Sun, Z. K. Zhou, C. W. Qiu, and X. H. Wang, "Full-colour nanoprint-hologram synchronous metasurface with arbitrary hue-saturation brightness control," Light Sci. Appl. **8**, 95 (2019).
11. M. J. Wan, Y. Li, J. W. Chen, W. Y. Wu, Z. Chen, Z. L. Wang, and H. T. Wang, "Strong tunable absorption enhancement in graphene using dielectric-metal core-shell resonators," Sci. Rep. **7**, 32 (2017).
12. Q. T. Cao, H. M. Wang, C. H. Dong, H. Jing, R. S. Liu, X. Chen, L. Ge, Q. H. Gong, and Y. F. Xiao, "Experimental demonstration of spontaneous chirality in a nonlinear microresonator," Phys. Rev. Lett. **118**, 033901 (2017).
13. Z. Shen, Y. L. Zhang, Y. Chen, C. L. Zou, Y. F. Xiao, X. B. Zou, F. W. Sun, G. C. Guo, and C. H. Dong, "Experimental realization of optomechanically induced non-reciprocity," Nat. Photonics **10**, 657–661 (2016).
14. J. C. Xue, Z. Z. Zhou, L. M. Lin, C. Guo, S. Sun, D. Y. Lei, C. W. Qiu, and X. H. Wang, "Perturbative countersurveillance metaoptics with compound nanosieves," Light Sci. Appl. **8**, 101 (2019).
15. P. Wang, A. V. Krasavin, M. E. Nasir, W. Dickson, and A. V. Zayats, "Reactive tunnel junctions in electrically driven plasmonic nanorod metamaterials," Nat. Nanotechnol. **13**, 159–164 (2018).
16. Z. Z. Zhou, J. Liu, Y. J. Bao, L. Wu, C. E. Png, X. H. Wang, and C. W. Qiu, "Quantum plasmonics get applied," Prog. Quantum Electron. **65**, 1–20 (2019).
17. K. Y. Yang, K. Beha, D. C. Cole, X. Yi, P. Del'Haye, H. Lee, J. Li, D. Y. Oh, S. A. Diddams, S. B. Papp, and K. J. Vahala, "Broadband dispersion-engineered microresonator on a chip," Nat. Photonics **10**, 316–320 (2016).
18. F. Yi, M. L. Ren, J. C. Reed, H. Zhu, J. C. Hou, C. H. Naylor, A. T. C. Johnson, R. Agarwal, and E. Cubukcu, "Optomechanical enhancement of doubly resonant 2D optical nonlinearity," Nano Lett. **16**, 1631–1636 (2016).
19. T. A. Voytova, A. V. Yulin, A. E. Krasnok, K. V. Baryshnikova, and P. A. Belov, "The role of Purcell effect for third harmonic generation," J. Phys. Conf. Ser. **690**, 012034 (2016).
20. P. N. Melentiev, A. E. Afanasiev, A. A. Kuzin, V. M. Gusev, O. N. Kompanets, R. O. Esenaliev, and V. I. Balykin, "Split hole resonator: a nanoscale UV light source," Nano Lett. **16**, 1138–1142 (2016).
21. A. Poddubny, I. Iorsh, P. Belov, and Y. S. Kivshar, "Hyperbolic metamaterials," Nat. Photonics **7**, 948–967 (2013).
22. L. Ferraria, C. Wub, D. Lepaged, X. Zhang, and Z. W. Liu, "Hyperbolic metamaterials and their applications," Prog. Quantum Electron **40**, 1–40 (2015).
23. I. Avrutsky, I. Salakhutdinov, J. Elser, and V. Podolskiy, "Highly confined optical modes in nanoscale metal-dielectric multilayers," Phys. Rev. B **75**, 241402 (2007).
24. G. Chen, H. Agren, T. Y. Ohulchanskyy, and P. N. Prasad, "Light upconverting core-shell nanostructures: nanophotonic control for emerging applications," Chem. Soc. Rev. **44**, 1680–1713 (2015).
25. X. Wu, Y. W. Zhang, K. Takle, O. Bilsel, Z. J. Li, H. Lee, Z. J. Zhang, D. S. Li, W. Fan, C. Y. Duan, E. M. Chan, C. Lois, Y. Xiang, and G. Han, "Dye sensitized core/active shell upconversion nanoparticles for optogenetics and bioimaging applications," ACS Nano **10**, 1060–1066 (2016).
26. B. Zhou, B. Shi, D. Jin, and X. Liu, "Controlling upconversion nanocrystals for emerging applications," Nat. Nanotechnol. **10**, 924–936 (2015).
27. S. Kruk, A. Poddubny, D. Smirnova, L. Wang, A. Slobozhanyuk, A. Shorokhov, I. Kravchenko, B. L. Davies, and Y. S. Kivshar, "Nonlinear light generation in topological nanostructures," Nat. Nanotechnol. **14**, 126–130 (2019).
28. A. F. Bravo, D. Q. Wang, E. S. Barnard, A. Teitelboim, C. Tajon, J. Guan, G. C. Schatz, B. E. Cohen, E. M. Chan, P. J. Schuck, and T. W. Odom, "Ultralow-threshold, continuous-wave upconverting lasing from subwavelength plasmons," Nat. Mater. **18**, 1172–1176 (2019).
29. S. H. Wen, J. J. Zhou, P. J. Schuck, Y. D. Suh, T. W. Schmidt, and D. Y. Jin, "Future and challenges for hybrid upconversion nanosystem," Nat. Photonics **13**, 828–838 (2019).
30. Y. Yi, Z. X. Chen, X. F. Yu, Z. K. Zhou, and J. Li, "Recent advances in quantum effects of 2D materials," Adv. Quantum Technol. **2**, 1800111 (2019).
31. F. Wang, R. Deng, and X. Liu, "Preparation of core-shell $NaGdF_4$ nanoparticles doped with luminescent lanthanide ions to be used as upconversion-based probes," Nat. Protoc. **9**, 1634–1644 (2014).
32. Z. Li and Y. Zhang, "An efficient and user-friendly method for the synthesis of hexagonal-phase $NaYF_4$:Yb, Er/Tm nanocrystals with controllable shape and upconversion fluorescence," Nanotechnology **19**, 345606 (2008).
33. Q. Zhan, H. Liu, and B. Wang, "Achieving high-efficiency emission depletion nanoscopy by employing cross relaxation in upconversion nanoparticles," Nat. Commun. **8**, 1058 (2017).
34. D. Lu, J. J. Kan, E. E. Fullerton, and Z. W. Liu, "Enhancing spontaneous emission rates of molecules using nanopatterned multilayer hyperbolic metamaterials," Nat. Nanotechnol. **9**, 48–54 (2014).
35. L. Li, W. Wang, T. S. Luk, X. D. Yang, and J. Gao, "Enhanced quantum dot spontaneous emission with multilayer metamaterial nanostructures," ACS Photon. **4**, 501–508 (2017).
36. A. P. Slobozhanyuk, P. Ginzburg, D. A. Powell, I. Iorsh, A. S. Shalin, P. Segovia, A. V. Krasavin, G. A. Wurtz, V. A. Podolskiy, P. A. Belov, and A. V. Zayat, "Purcell effect in hyperbolic metamaterial resonators," Phys. Rev. B **92**, 195127 (2015).
37. A. V. Chebykin, V. E. Babicheva, I. V. Iorsh, A. A. Orlov, P. A. Belov, and S. V. Zhukovsky, "Enhancement of the Purcell factor in multiperiodic hyperbolic like metamaterials," Phys. Rev. A **93**, 033855 (2016).
38. Y. F. Shen, Y. X. Yan, A. N. Brigeman, H. Kim, and N. C. Giebink, "Efficient upper-excited state fluorescence in an organic hyperbolic metamaterial," Nano Lett. **18**, 1693–1698 (2018).
39. Z. K. Zhou, J. C. Xue, Z. B. Zheng, J. H. Li, Y. L. Ke, Y. Yu, J. B. Han, W. G. Xie, S. Z. Deng, H. J. Chen, and X. H. Wang, "A centimeter-scale sub-10 nm gap plasmonic nanorod array film as a versatile platform for enhancing light-matter interactions," Nanoscale **7**, 15392–15403 (2015).
40. A. V. Kachynski, A. Pliss, A. N. Kuzmin, T. Y. Ohulchanskyy, A. Baev, J. Qu, and P. N. Prasad, "Photodynamic therapy by *in situ* nonlinear photon conversion," Nat. Photonics **8**, 455–461 (2014).
41. H. Zhang, T. Jia, X. Shang, S. Zhang, Z. Sun, and J. Qiu, "Mechanisms of the blue emission of $NaYF_4$:Tm^{3+} nanoparticles excited by an 800 nm continuous wave laser," Phys. Chem. Chem. Phys **18**, 25905–25914 (2016).
42. G. F. Wang, W. P. Qin, L. L. Wang, G. D. Wei, P. F. Zhu, and R. J. Kim, "Intense ultraviolet upconversion luminescence from hexagonal $NaYF_4$:Yb^{3+}/Tm^{3+} microcrystals," Opt. Express **16**, 11907–11914 (2008).
43. D. A. Simpson, W. E. K. Gibbs, S. F. Collins, W. Blanc, B. Dussardier, G. Monnom, P. Peterka, and G. W. Baxter, "Visible and near infra-red up-conversion in Tm^{3+}/Yb^{3+} co-doped silica fibers under 980 nm excitation," Opt. Express **16**, 13781–13799 (2008).
44. J. Liao, D. Jin, C. Chen, Y. Li, and J. Zhou, "Helix shape power dependent properties of single upconversion nanoparticles," J. Phys. Chem. Lett. **11**, 2883–2890 (2020).
45. K. R. Deng, L. L. Xu, X. Guo, X. T. Wu, Y. L. Liu, Z. M. Zhu, Q. Li, Q. Q. Zhan, C. X. Li, and Z. W. Quan, "Binary nanoparticle superlattices for plasmonically modulating upconversion luminescence," Small **16**, 2002066 (2020).
46. Z. F. Liao, H. F. Xu, W. R. Zhao, H. X. Yang, J. Y. Zhong, H. Zhang, Z. G. Nie, and Z. K. Zhou, "Energy transfer from Mn^{4+} to Mn^{5+} and near infrared emission with wide excitation band in $Ca_{14}Zn_6Ga_{10}O_{35}$:Mn phosphors," Chem. Eng. J. **395**, 125060 (2020).

47. J. G. Danzl, S. C. Sidenstein, C. Gregor, N. T. Urban, P. Ilgen, S. Jakobs, and S. W. Hell, "Coordinate-targeted fluorescence nanoscopy with multiple off states," Nat. Photonics **10**, 122–128 (2016).
48. Y. M. Wu, J. H. Xu, E. T. Poh, L. L. Liang, H. L. Liu, J. K. W. Yang, C. W. Qiu, R. A. L. Vallée, and X. G. Liu, "Upconversion superburst with sub-2 μs lifetime," Nat. Nanotechnol. **14**, 1110–1115 (2019).
49. J. J. Zhou, S. H. Wen, J. Y. Liao, C. Clarke, S. A. Tawfik, W. Ren, C. Mi, F. Wang, and D. Y. Jin, "Activation of the surface dark-layer to enhance upconversion in a thermal field," Nat. Photonics **12**, 154–158 (2018).
50. D. W. Lu, S. K. Cho, S. Ahn, L. Brun, C. J. Summers, and W. H. Park, "Plasmon enhancement mechanism for the upconversion processes in $NaYF_4$:Yb^{3+}, Er^{3+} nanoparticles: Maxwell versus Förster," ACS Nano **8**, 7780–7792 (2014).
51. B. Zhou, B. Tang, C. Zhang, C. Y. Qin, Z. J. Gu, Y. M. Ma, T. Y. Zhai, and J. N. Yao, "Enhancing multiphoton upconversion through interfacial energy transfer in multilayered nanoparticles," Nat. Commun. **11**, 1174 (2020).
52. D. Li, B. Dong, X. Bai, Y. Wang, and H. W. Song, "Influence of the TGA modification on upconversion luminescence of hexagonal-phase $NaYF_4$:Yb^{3+}, Er^{3+} nanoparticles," J. Phys. Chem. C **114**, 8219–8226 (2010).
53. Q. Zhan, X. Zhang, Y. Zhao, J. Liu, and S. He, "Tens of thousands-fold upconversion luminescence enhancement induced by a single gold nanorod," Laser Photon. Rev. **9**, 479–487 (2015).